Researchers Journal of Science and Technology (REJOST)
https://rejost.com.ng

Comparative Ab-Initio Investigation of Structural, Electronic, Mechanical, Thermoelectric and Thermophysical Properties of MnAs Polymorphs

C. U. Akpanmbai, S. A. Ekong*, J. B. Emah

Abstract

Intermetallic compounds are ordered solid-state metallic alloys which are widely used in aerospace, energy and electronic industries, and are crucial for high-temperature structural components in aircraft engines. The present study investigates MnAs intermetallics via ab-initio structural, electronic, mechanical, thermoelectric and thermophysical properties using density functional theory (DFT) with PBEsol exchange–correlation functional. This investigation was centered on the tetragonal (Tetr), hexagonal (hcp), and cubic (cP) phases of MnAs. The novelty of this investigation lies in its thermoelectric analysis, which has not yet been reported in scientific literature. Our computed lattice parameters of $a_0 = 3.70$ Å and $c_0 = 6.17$ Å (for Tetr phase), $a_0 = 3.65$ Å and $c_0 = 5.60$ Å (for hcp phase), and $a_0 = 5.69$ Å (for cP phase) aligns well with experiment and existing theoretical data, indicating the validity of the study. The negative formation energy and binding energy analysis showcases the structural stability of the calculations. The electronic density of states calculations revealed zero band gap energy as an indication that all three phases are metallic conductors. The obtained elastic constants for the Tetr, hcp, and cP phases of MnAs satisfy the Born mechanical stability criteria, suggesting that all three phases are mechanically stable. Significantly, the mechanical analysis from B_H/G_H ratio and Poisson's ratio exhibited ductility, which confirms the electronic DOS results of the three phases as metals. Also, while they all exhibit anisotropic character, the highest resistant to deformation is found in Tetr and hcp phases. Furthermore, the investigated thermoelectric (TE) transport properties recorded maximum power factors of 4.4 x 10^{11} W.cm^{-1}.K^{-2}.s^{-1} (Tetr phase), 7.2 x 10^{11} W.cm^{-1}.K^{-2}.s^{-1} (hcp phase), and 9.4 x 10^{11} W.cm^{-1}.K^{-2}.s^{-1} (cP phase) all at 800 K respectively. Moreover, our finding suggests that the registered high Seebeck coefficient S and minimum thermal conductivity k_e displayed by the cP phase at 300 K makes this

phase a promising candidate for TE applications. The thermophysical assessment of the Debye temperature, entropy, free energy, internal energy, heat capacity, and acoustic sound velocities of Tetr, hcp, and cP compounds of MnAs are also discussed.

✉ S. A. Ekong: sylvesterekong@aksu.edu.ng

Department of Physics, Akwa Ibom State University, Ikot Akpaden, P.M.B. 1167, Uyo, Nigeria.

Keywords: MnAs phases, Electronic, Thermoelectric, Mechanical, Thermophysical properties

Article history

Received: December 28, 2025
Received in revised form: January 27, 2026
Accepted for publication: February 1, 2026
Available online: February 3, 2026

1.0 Introduction

Intermetallic compounds (IMCs) are ordered, metallic compounds with unique structural characteristics, formed from two or more metallic elements. IMCs offer a rich and diverse resource for materials studies related to chemical composition and other physical properties (Gourdon *et al*., 2016). Their electronic states provide insights into the chemical bonding factors influencing composition and structure, as well as the electronic underpinnings of electrical and magnetic behaviors. They are often hard and brittle but possess excellent high-temperature properties, making them valuable for applications such as wear-resistant coatings, cutting tools, and structural materials in high-performance environments (Yu & Liu, 2025). In recent years, the study of the physical and transport properties of IMCs has emerged as a central area of focus in materials engineering (Yu *et al.*, 2025; Li *et al.*, 2024; Tolochyn *et al*., 2021). This surge in interest is largely attributed to the pivotal role these materials play in influencing the efficiency, reliability, and performance of electronic device interconnections (Yu & Liu, 2025). Among the various IMCs, the manganese arsenide (MnAs) system has attracted substantial attention, particularly for its relevance to applications such as magnetic storage memory, magnetic refrigerants, and galvanomagnetic properties (Habiba *et al*., 2020; Saypulaeva *et al.,* 2019). Within the material's polymorphs, experiments have reported the structural and electronic properties of the hexagonal, cubic, monoclinic, tetragonal, and orthorhombic phases of MnAs (Marenkin *et al.*, 2018; Gama & Cardoso, 2006; Hagedorn & Jeitschko, 1995). MnAs being an original magnetic material is suitable for spin-electronic and magneto-optic applications (Moradiannejad *et al*., 2013). The properties of the NiAs and MnP type structures were experimentally investigated while that of the zinc-blend structure are theoretically predicted (Hayashi *et al*., 2001; Ohno, 1999). They are ferromagnetic in the NiAs-type crystal structure at 318 K (Arejdal *et al*., 2017; Tocado *et al*., 2009), and has been reported for half-metallicity (Paiva *et al*., 2004; Sanvito & Hill, 2000) in the zinc-blende structure (Moradiannejad *et al*., 2013). At pressures beyond 0.4 GPa, experimental observations showed a structural transition to the MnP-type structure and a further magnetic transition to a mixed ferromagnetic and anti-ferromagnetic phase (Sanvito & Hill, 2000; Maki *et al*., 1998). Due to its ferromagnetic low-temperature properties, the NiAs-type hexagonal phase has attracted greater attention from experimental and theoretical investigations (Habiba *et al*., 2020; Algarni *et al.*, 2020; Saypulaeva *et al.,* 2019; Marenkin *et al.*, 2018). Consequently, the behavioral characteristics of the hexagonal phase, such as electronic and structural properties, optical spectra, magnetization, thermal, and dynamical properties, are well documented in the literature.

Nevertheless, apart from the meager reported electronic and structural properties from experiments on the other phases of MnAs, their

elastic, mechanical, thermodynamic, and dynamical properties remain scarce in the literature. To the best of our knowledge, the thermophysical properties of the tetragonal and cubic phases of MnAs intermetallic alloys are scarce in the literature. Furthermore, no scientific investigation of the thermoelectric (TE) transport properties of any phase of MnAs has yet been reported in the literature. The current investigation aims to close research gaps, particularly for the tetragonal (Tetr) and cubic (cP) phases of MnAs regarding TE transport properties. This work assesses the tetragonal, hexagonal, and cubic phases of MnAs by comparing their structural, electronic, thermoelectric, mechanical, and thermophysical properties. The method of ab initio density functional theory (DFT) has been praised for yielding results in good agreement with experiment (Hayat *et al.*, 2025; Jolayemi *et al.*, 2020; Ekong *et al.*, 2015). Hence, this investigation employs the DFT formalism. Our results demonstrate not only the structural and energetic stability of the three MnAs phases, in agreement with experiment, but also provide significant insights into their binding energies and TE transport characteristics. Knowing that there were no usable experimental data on TE properties, the current predictions are now the available theoretical results and are open to experimental validation. Moreover, in the current contribution, it is found that among the three phases, the cubic (cP) phase yields the highest power factor (PF), which is attributed to its lowest thermal conductivity (see Fig. 6(c)). This contribution establishes a benchmark for the computational modeling of other MnAs intermetallics for future experimental and device-level studies.

2.0 Theory and Computational Methods

The electronic, mechanical, thermophysical, and thermoelectric properties for tetragonal (Tetr), hexagonal (hcp) and cubic (cP) phases of MnAs intermetallic crystal are performed in the framework of density functional theory (DFT), a quantum mechanical modelling technique, within the quantum ESPRESSO (QE) simulation package (Giannozzi *et al.*, 2017). For improved equilibrium parameters, the PBEsol (Espinosa-García *et al.*, 2011), being a revised Perdew-Burke-Ernzerhof generalized gradient approximation (GGA) used for many densely packed solids and their surface calculations, is adopted for this investigation. The mesh cutoff energy for separating valence and core states is chosen as 90 Ry (Tetr), 110 Ry (hcp), and 65 Ry (cP). Also, Monkhorst-Pack k-point meshes of 12 x 12 x 7 (Tetr), 13 x 13 x 8 (hcp), and 8 x 8 x 8 (cP) were adopted for the investigations. Performing a self-consistent-field (scf) test by varying the experimental lattice parameters for Tetr phase: a_0 = 3.77 Å and c_0 = 6.28 Å (Marenkin *et al.*, 2018), for hcp phase: a_0 = 3.70 Å and c_0 = 5.70 Å (Sanvito & Hill, 2000), and for cP phase: a_0 = 5.74 Å (Qian *et al.*, 2004). The structural optimization test for the conventional Wyckoff positions was done by varying the lattice parameters between $-0.5 \leq a_0 \leq 0.5$ at a step of 0.1, and interpolating with the energy, the material's optimal lattice parameters were determined. Additionally, calculations of the density of state (DOS) and projected DOS used twice the k-points grid for optimal representations. For geometry optimizations, the total energy convergence threshold was set to 1 x 10^{-6} Ry/atom with a gaussian broadening width of 0.002 Ry respectively. All structures have been relaxed based on Broyden-Fletcher-Goldfarb-Shanno (BFGS) algorithm (Osorio-Guillén *et al.*, 2012) for stress minimization. The force on atoms is less than 1.0 mRy/Å. The unit cells of the MnAs intermetallic alloys consisted of six atoms (Tetr), four atoms (hcp), and eight atoms (cP), with corresponding space groups in order of P4/nmm (Tetr), $P6_3/mmc$ (hcp), and $F\bar{4}3m$ (cP). The elastic constants (C_{ij}) of the alloys are studied using thermo-pw code (Malica & Corso, 2020). The applied stress σ to strain (ε) is expressed as:

$$\sigma_{ij} = \sum_{k,l=1}^{6} C_{ijkl}\varepsilon_{kl} \qquad (1)$$

where C is the modulus of elasticity or elastic constant. The dependence of strain and total energy using Voigt-Reuss-Hill (VRH) approximation scheme (Hill, 1952; Reuss, 1929; Voigt, 1928; 1910) was adopted to accomplish the task of materials deformation tensors. The mechanical stability criteria to be satisfied according to (Mouhat & Couder, 2014; Born *et al.*, 1955) are given as:

$$\textbf{Tetr: } C_{11}+C_{33}-2C_{13}>0;\ 2(C_{11}+C_{12})+C_{33}+4C_{13}>0;\quad C_{11}-C_{12}>0, \tag{2a}$$

$$\textbf{hcp: } C_{11}-|C_{12}|>0\ ;\qquad (C_{11}+C_{12})\,C_{33}-2C_{13}^{2}>0;\ C_{44}>0 \tag{2b}$$

$$\textbf{cP: } C_{11}+2C_{12}>0,\ C_{11}-C_{12}>0,\ C_{44}>0 \tag{2c}$$

Additionally, thermodynamic parameters are processed based on quasi-harmonic approximations (QHA) (Aniefiok *et al.*, 2025; Baroni *et al.*, 2010). Transport properties such as the Seebeck coefficient, electrical conductivity, and power factor are determine using BoltzTrap program patch (Madsen & Singh, 2006) as an interface with QE. Based on this Boltzmann semi-classical theory, calculations were performed on temperatures ranging from 300 to 800 K with chemical potentials of (–0.15 to +0.15 Ry) respectively. According to the semi-classical Boltzmann transport equation (BTE), the Seebeck coefficient, electrical conductivity, and thermal conductivity tensors are expressed as (Khan *et al.*, 2017):

$$S = ek_B\sigma^{-1}\sum \mathrm{k}\left(-\frac{\mathrm{df_E}}{\mathrm{d\varepsilon}}\right)\mathrm{v_k^2}\tau_\mathrm{k}\left(\frac{\mathrm{k_B}-\chi}{\mathrm{k_B T}}\right) \tag{3}$$

$$\sigma = \mathrm{e}^2\sum \mathrm{k}\left(-\frac{\mathrm{df_E}}{\mathrm{d\varepsilon}}\right)\mathrm{v_k^2}\tau_\mathrm{k} \tag{4}$$

$$k_e = ek_B\sigma^{-1}\sum \mathrm{k}\left(-\frac{\mathrm{df_E}}{\mathrm{d\varepsilon}}\right)\mathrm{v_k^2}\tau_\mathrm{k}\left(\frac{\mathrm{k_B}-\chi}{\mathrm{k_B T}}\right) - T\sigma S^2 \tag{5}$$

where f_E is the Fermi function, V_k is for the group velocity, k_B denotes the Boltzmann constant, τ_k represents the relaxation time, k is the wave vector and χ denotes the chemical potential. Adopting Eqs. (3) – (5), the TE or transport coefficients of the compounds are thus calculated.

3.0 Results and Discussion

3.1 Structural and Energetical Stability

The optimized crystal structures for the tetragonal (Tetr), hexagonal (hcp), and cubic (cP) phases of MnAs intermetallic alloys are shown in Fig. 1(a), (c), (e), respectively. In Fig. 1(a), each As-atom is located on the z-directional site and is bonded hexagonally to Mn-atoms. In Fig. 1(c), the As-atoms are bonded internally and hexagonally to Mn-atoms. In Fig. 1(e), firstly, the As-atoms form double hexagonal cyclic chains with Mn-atoms, and secondly, each As-atom is bonded tetragonally to Mn atoms of the cP phase. Also, illustrated in Fig. 1((b), (d), (f)) are the total energy as a function of unit cell volume (E-V) plots obtained by fitting the E-V data into Eq. (6) for the Tetr, hcp, and cP phases. The minimum total energy (E_0) accounts for the bound states of a material, and is estimated using the Murnaghan equation of state (EoS) expressed as (Murnaghan, 1944; Ekong *et al.*, 2014):

$$E(V) = E_0 + \frac{B_0 V}{B_P(B_P-1)}\left[\left(\left(\frac{V_0}{V}\right)^{B_P}-1\right)+B_P\left(1-\left(\frac{V_0}{V}\right)\right)\right] \tag{6}$$

Here, V_0 is the equilibrium volume, B_0 is the bulk modulus, and B_P is the first pressure derivative of B0. The pattern exhibited by the E–V curves in Fig. 1((b), (d), (f)) for the $E0$ shows that the cP phase in Fig. 1(f) is the most stable compared to the others by exhibiting the lowest bound state energy, which follows the order of cP (-916.52 Ry) < Tetr (-880.61 Ry) < hcp (-458.51 Ry) as revealed in Table 1. Also, presented in Table 1 are other calculated structural properties of the Tetr, hcp, and cP phases of MnAs, including the lattice parameters (a_0, c_0), formation energy ($E_{form.}$), and binding energy (E_B). Focusing on structural analysis and comparison with available experimental data, the calculated lattice parameters revealed a systematic variation due to structural differences. The a_0-parameter decreases from 3.70 Å (Tetr) to 3.65 Å (hcp) and then increases

to 5.69 Å (cP). The c_0-parameter showed a similar trend from 6.17 Å (Tetr) to 5.60 Å (hcp). These changes reflect the increasing unit cell size of each phase owing to the number of atoms per unit cell, as mentioned in section 2. Compared to experimental values in Table 1, the relative deviations for lattice parameters are as follows: Tetr: a_0 = 1.86%, c_0 = 1.75%, hcp: a_0 = 1.35%, c_0 = 1.75%, cP: a_0 = 0.87%. These discrepancies are within expected limits and are typical of GGA-based calculations, which slightly underestimate lattice dimensions (Chenafi *et al*., 2025; Jolayemi *et al*., 2019). This minor variation across the three MnAs compounds indicates structural robustness and symmetry preservation, regardless of the MnAs intermetallic phase. In summary, the structural properties of each phase exhibit consistent trends with unit cell size, in the order cP > Tetr > hcp, and show good agreement with experimental data, confirming the accuracy of the calculated results. Furthermore, in Table 1, the calculated first pressure derivative indicated approximate compressibilities of 6.0 for both the Tetr and hcp phases and 15 for the cP phase, indicating significant resistance to compression of the cP phase under external force.

Meanwhile, the energetical stability analysis can be revealed from the minimum energy (E_0), formation energy ($E_{form.}$), and binding energy (E_B) calculations. Moreso, while the $E_{form.}$ indicates the energy gain in assembling the alloys, the E_B illustrates the energy required to disassemble the system into its individual components, and they are represented in Eq. (7) and Eq. (8) as (Balaji *et al*., 2025):

$$E_{form.} = \frac{1}{N}[E_{MnAs} - n_{Mn} * E_{Mn} - n_{As} * E_{As}] \quad (7)$$

$$E_B = \frac{1}{N}[\mu_{MnAs} - n_{Mn} * \mu_{Mn} - n_{As} * \mu_{As}] \quad (8)$$

In this context, E_{MnAs} signifies the overall total energy of the systems, while n_{Mn} , n_{As} , E_{Mn} and E_{As} denotes the numbers and energies of individual atoms, and N is the total number of all the atoms. The variable 'μ' symbolizes the free energy of the compounds in similar order. Using Eqs. (7) and (8), the computed values of $E_{form.}$ and E_B are given in Table 1. The overall E_B values vary from −0.27 eV to −0.30 eV, while that of $E_{form.}$ ranges from −0.19 eV to −0.24 eV. The alignment of our computed binding and formation energies for stability has no previous study to compare with. However, higher negative values indicate greater stability. In this analysis, the negative values obtained for both $E_{form.}$ and E_B are indications that the materials can be reproduced experimentally. Also, unlike the two other MnAs phases, the cubic cP phase has a more stable $E_{form.}$ (−0.24 eV) and E_B (−0.30 eV), making it the most energetically stable phase. These findings validate the computational model and provide a solid basis for further analysis of mechanical and electronic evaluations.

3.2 Electronic Properties

The density of states (DOS), the number of available states within a system in the energy interval (E + dE), reflects the energy-level structure of a material and aids in the analysis of elemental interactions. Presented in Fig. 2 are the Total-DOS and projected-DOS (PDOS) of the three phases of MnAs under consideration. In the profile of the Total-DOS and PDOS, the left panel indicates the valence bands, while the right panel represents the conduction bands, both separated by a vertical red dotted line – Fermi level. In Fig. 2, the profile clearly shows that the valence bands (VBs) have a higher density of states than the conduction bands (CBs). An extensive examination of the Total-DOS for Tetr: Fig. 2(a1), hcp: Fig. 2(b1), and cP: Fig. 2(c1) and the PDOS (Tetr: Fig. 2(a2), hcp: Fig. 2(b2), and cP: Fig. 2(c2)) curves in this investigation reveals discernible characteristics in their VBs, likewise the CBs of the alloy compounds. The Total-DOS curves revealed two distinct lacunas within the VBs in regions of -5.5 to -5 eV and -3 to -2.5 eV (in Fig. 2(a1)), -4 to -3.5 eV and -2 to -1.5 eV (in Fig. 2(b1)), and in Fig. 2(c1) with -3 to -2.8 eV and -1.6 to -0.5 eV.

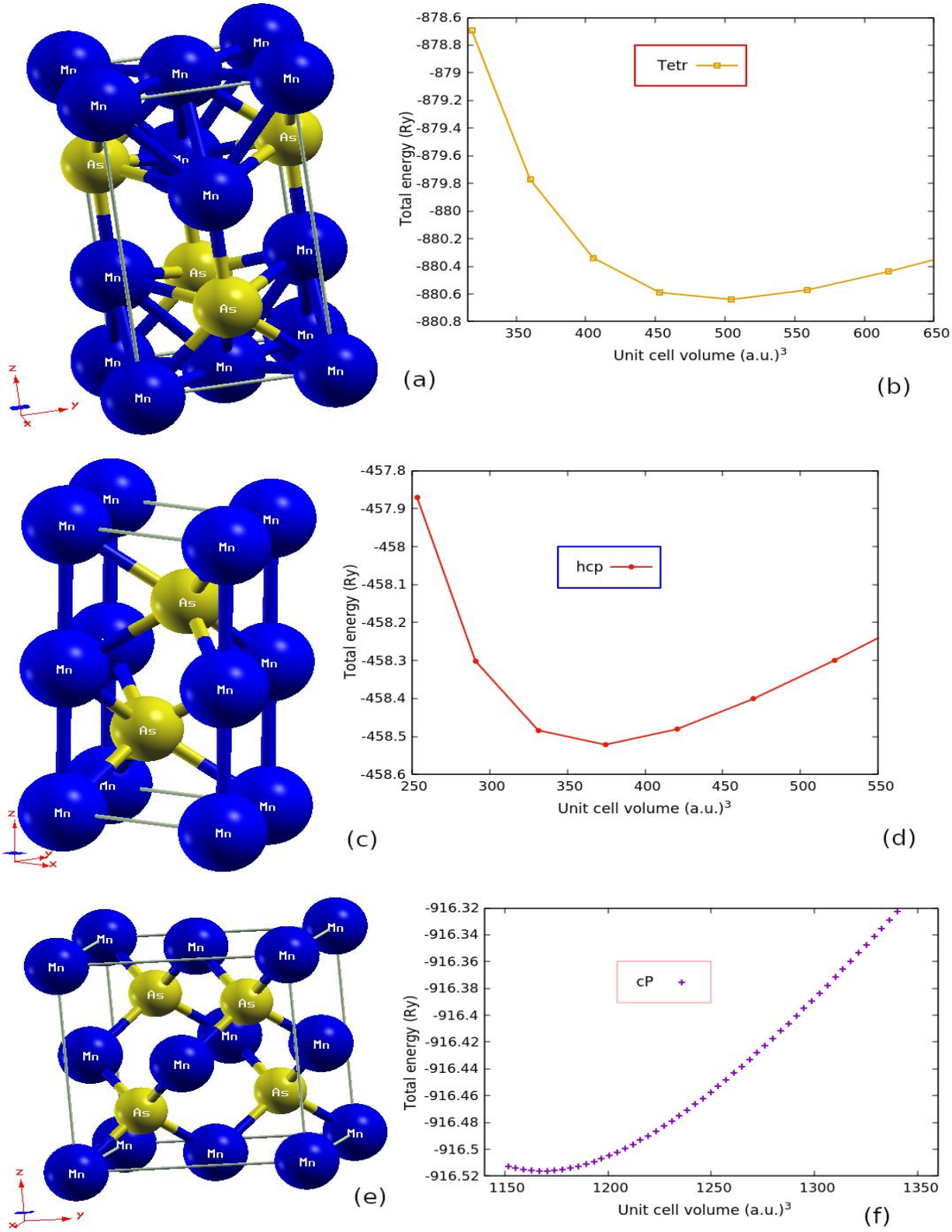

Fig. 1: Crystal structure and energy–volume (E–V) dependent plots of tetragonal (top panel), hexagonal (middle panel) and cubic (bottom panel) phases of MnAs intermetallic alloys

Similarly, the CBs regions, although with shorter energy range, display the same trends, which are distinctly apparent at about 0.9 to 1.3 eV, 0.8 to 1.0 eV, and 0.7 to 1.1 eV. Moreover, in Fig. 2, it can be seen that within the Fermi level, the different phases exhibit metallic behavior, as no energy band gap is present. Also, materials that exhibit good electrical conductivity display a sharp, high slope in the Total-DOS near the Fermi level, and consequently serve as a hint for

the search for promising thermoelectric (TE) materials (Chen *et al*., 2021). In light of this, the compound that suits the above description most is the cP phase of Fig. 2(c1, c2). Meanwhile, considering the valence states of Mn ($4s^2 3d^5$) and As ($4s^2 4p^3$), it is apparent in the PDOS profiles that the dominant contributions to electronic transfer from the VBs to CBs come from the 4*d*- and 2*p*-orbitals. However, the meager contributions of the s-orbitals are particularly conspicuous in the VBs segment. Interestingly, the zero-energy gaps elucidated by each phase offer a more refined insight into the electronic nature of the compounds.

Table 1: Optimized lattice parameters (a_0 and c_0, in Å), equilibrium volume V_0 (in Å^3), bulk modulus B_0 (in GPa), first pressure derivative of bulk modulus B_p, minimum total energy E_0 (in Ry), formation energy $E_{form.}$ (in eV/atom) and binding energy E_B (in eV/atom) of tetragonal, hexagonal and cubic phases of MnAs crystal structures

References	a_0	c_0	$\frac{c_0}{a_0}$	V_0	B_0	B_P	E_0	$E_{form.}$	E_B
				Tetragonal	**Phase**				
This work	3.70	6.17	1.67	74.16	257.70	5.86	-880.61	-0.21	-0.29
[a]Expt	3.77	6.28	1.67	-	-	-	-	-	-
				Hexagonal	**Phase**				
This work	3.65	5.60	1.53	54.52	196.90	6.05	-458.51	-0.19	-0.27
[b]Theory	3.70	5.70	1.53	-	-	-	-	-	-
[a]Expt	3.73	5.70	1.53	-	-	-	-	-	-
[c]Expt	3.72	5.70	1.53	-	-	-	-	-	-
[d]Expt.	3.70	5.70	1.54	53.03	-	-	-	-	-
				Cubic	**Phase**				
This work	5.69	-	-	173.08	423.20	15.00	-916.52	-0.24	-0.30
[e]Expt.	5.74	-	-	-	-	-	-	-	-

[a]Expt. – (Marenkin *et al*., 2018); [b]Theory – (Algarni *et al*., 2020); [c]Expt. – (Moradiannejad *et al*., 2013)
[d]Expt. – (Sanvito & Hill, 2000); [e]Expt. – (Qian *et al*., 2004)

The detailed PDOS analysis not only highlights the overall distribution of states but also pinpoints specific orbital contributions responsible for the observed electronic characteristics. Significantly, an examination of the three MnAs phases revealed that, unlike the cP phase, the Tetr and hcp phases exhibit a decrease in the difference between the lowest and highest VBs. This again could have important consequences for their electronic transport properties. Lastly, observations from Fig. 2 revealed an increased range of energy within the VBs region and a narrower range within the CBs region. Therefore, it is logical to infer that the VB profile for the cP phase displays a clear singularity slightly below the Fermi level, leading to a higher DOS and suggesting an enhanced charge-carrier concentration, which makes it a superior candidate for electronic transport applications compared to its counterparts.

3.3 Elastic and Mechanical Analysis

In addition to structural stability, the mechanical properties of the tetragonal (Tetr), hexagonal (hcp), and cubic (cP) phases of the compounds were examined to assess their potential for applications where both resilience and flexibility are essential. Studying the mechanical behavior of materials has industrial applications, as it provides material information about how materials respond to external strain. Such characteristic properties are often obtained from calculations of elastic constants (C_{ij}) to support applications in which materials experience stress and strain during loading and unloading. Elastic properties can significantly influence the design, performance, and safety of materials. Properties

such as Young's modulus, shear modulus, bulk modulus, Poisson's ratio, and Pugh's ratio (B_H/G_H) provide insights into a material's ability to withstand deformation under external forces. To ensure structural integrity and materials stability, understanding these properties is crucial. Our computed elastic constants, C_{ij}, using the stress-strain method of the VRH (Hill,1952) schemes for the MnAs phases are given in Table 2. Obviously, the obtained elastic constants align with the requirement of the Born stability criteria (Born *et al*., 1955) mentioned above.

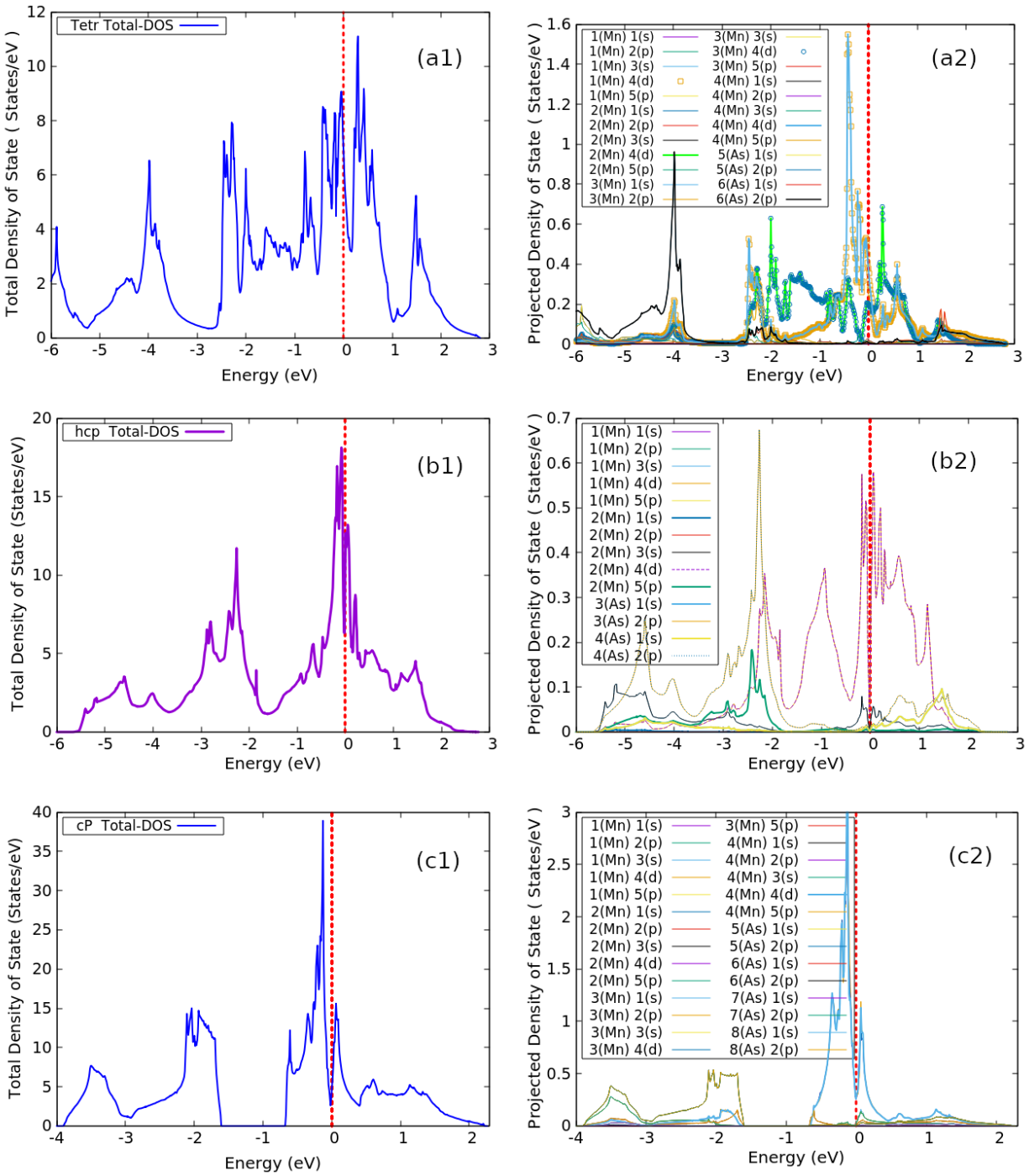

Fig. 2: Energy dependence plots of total density of state (Total DOS) and projected density of states (PDOS) of the Tetr phase: Fig. 2(a1 and a2), hcp phase: Fig. 2(b1 and b2), and cP phase Fig. 2(c1 and c2) of MnAs alloys. The dotted-red line denotes the Fermi energy level.

Table 2: Elastic constants (C*ij*) in GPa

Materials	C_{11}	C_{12}	C_{13}	C_{33}	C_{44}	C_{66}	Ref.
Tetr	264.97	116.93	152.49	363.49	57.35	58.61	This work
Hcp	170.76	108.10	23.01	136.24	140.96	31.33	This work
cP	74.10	48.09	-	-	7.35	-	This work

Observations from Table 2 revealed that the resistive strength of each phase is highest in the axis of C_{33} plane in the {111} direction (for Tetr phase), C_{11} plane in the {100} direction (for hcp phase), and C_{11} plane in the {100} direction (for cP phase). For the hcp phase, the $C_{66} = (C_{11} - C_{12})/2$. Consequently, the C_{66} represents the tolerance to shear in the {100} plane in the [110] direction, while the C_{44} represents the tolerance to shear in the {010} or {100} plane in the [001] direction. Moreover, the values of C_{11} and C_{33} are larger than those of C_{44} and C_{66}, suggesting that these compounds are more incompressible under uniaxial stress along the *x*- and *z*-axes. Based on the VRH scheme, the calculated bulk modulus (B_V, B_R, B_H), shear modulus (G_V, G_R, G_H), Young's modulus (E_V, E_R, E_H), and other mechanical parameters are summarized in Table 3. The calculated bulk (B_V, B_R) and shear (G_V, G_R) moduli based on the Voigt (V) and Reuss (R) approximation scheme for the different phases are as follows. For Tetragonal (Tetr) phase (Omboga et al., 2020):

$$B_V = (2C_{11} + 2C_{12} + 4C_{13} + C_{33})/9 \quad \text{and} \quad B_R = \frac{(C_{11} + C_{12})C_{33} - 2C_{13}^2}{C_{11} + C_{12} - 4C_{13} + 2C_{33}} \tag{9}$$

Also,
$$G_V = (4C_{11} + 2C_{33} - 4C_{13} - 2C_{12} + 12C_{44} + 6C_{66})/30 \tag{10}$$

$$G_R = \left[\frac{18B_V}{(C_{11} + C_{12})C_{33} - 2C_{13}^2} + \frac{6}{C_{11} - C_{12}} + \frac{6}{C_{44}} + \frac{3}{C_{66}}\right]^{-1} \tag{11}$$

For Hexagonal (hcp) phase (Zeng *et al*., 2018):

$$B_V = 2(C_{11} + C_{12} + 2C_{13} + 0.5C_{33})/9 \quad \text{and} \quad B_R = \frac{(C_{11} + C_{12})C_{33} - 2C_{13}^2}{C_{11} + C_{12} - 4C_{13} + 2C_{33}} \tag{12}$$

Again,
$$G_V = (7C_{11} - 5C_{12} + 2C_{33} - 4C_{13} + 12C_{44})/30 \tag{13}$$

$$G_R = \frac{5}{2}\left[\frac{\{(C_{11}+C_{12})C_{33} - 2C_{33}\}C_{44}C_{66}}{3\,B_V\,C_{44}\,C_{66} + \{(C_{11}+C_{12})C_{33} - 2C_{13}^2\}(C_{44} + C_{66})}\right] \tag{14}$$

For the cubic (cP) phase (Gregory *et al*., 2024):

$$\mathrm{B_V} = \frac{1}{3}C_{11} + \frac{2}{3}C_{12}; \quad \mathrm{B_R} = \frac{1}{3S_{11} + 6S_{12}} \tag{15}$$

and

$$\mathrm{G_V} = \frac{1}{5}(C_{11} - C_{12}) + \frac{3}{5}C_{44}; \quad \frac{5}{\mathrm{G_R}} = \frac{4}{C_{11} - C_{12}} + \frac{3}{C_{44}} \tag{16}$$

where C_{ij} and S_{ij} are the respective elastic constants and elastic compliances. Therefore, the Voigt-Reuss-Hill (VRH) scheme averages the bulk and shear moduli as (Ekong *et al*., 2025; Zeng *et al*., 2018):

$$B_H = (B_V + B_R)/2 \text{ and } G_H = (G_V + G_R)/2 \tag{17}$$

The adoption of Eq. (9) yields Young's modulus ($\mathbf{E}_H$) and Piosson's ratio ($\mathbf{V}_H$) given as follows:

$$\mathbf{E}_H = \frac{9\,B_H\,G_H}{3B_H + G_H} \text{ and } \mathbf{V}_H = \frac{3B_H - 2G_H}{2(3B_H + G_H)} \tag{18}$$

$$A^U = \frac{5G_V}{G_R} + \frac{B_V}{G_R} - 6 \quad (19)$$

The results of Table 3 reveal a higher Young's modulus E_H in Tetr and hcp phases compared to the cP phase. This showcases the high mechanical stiffness to elastic deformation under lengthwise force in Tetr and hcp phases. Also, the ductility or brittleness of Tetr, hcp, and cP phases of MnAs is evaluated according to Pugh's ratio (B_H/G_H) (Pugh, 1954) and Poisson's ratio (V_H) (Greaves *et al*., 2011). Accordingly, the standard criteria for a material's Poisson's ratio reflects brittleness if $V_H < 0.31$ or ductility if $V_H \leq 0.5$, while that of Pugh's ratio (B_H/G_H) signature brittleness < 1.75 < ductility. In Table 3, the calculated V_H values show that all three phases lie within the range of 0.31 – 0.42, and it is concluded that they all exhibit ductility, which confirms the electronic DOS results in Fig. 2.

In addition, the obtained values of B_H/G_H further confirm the ductile nature of the MnAs phases. We clearly notice that the same conclusion for B_H/G_H has been reached for E_H such that, as the value of B_H/G_H decreases the stiffness E_H of the compounds increases and vice versa. The calculations of the anisotropy/isotropy parameters like the Universal anisotropy index (A^U) in Eq. (19), anisotropy indices of shear (A^G) and bulk (A^B), scalar log-Euclidean anisotropy index (A^L), and Zener anisotropy factor (A^z) moduli are detailed elsewhere (Luan *et al*., 2018; Zeng *et al*., 2018). In isotropic materials, the values of A^U, A^B, A^G, and A^L must be zero, whereas a value of 1 (one) is required in the case of A^Z. Any deviation from these values reflects the degree of elastic anisotropy. The calculated results of A^U, A^B, A^G, A^L, and A^Z, as presented in Table 3, showed a distinction from zero and 1 (one), signaling elastic anisotropy for all three phases. Observation reveals that the shear anisotropy of the MnAs phases is more significant than the compressibility anisotropy.

Anisotropy information in materials is essential for showcasing mechanical performance in real-world applications (Gaillac *et al*., 2016; Ranganathan *et al*., 2008). In Fig. 3 and Fig. 4, the 3D directional and xy–surface dependency of Young's modulus and Poisson's ratio plots produced with the ELATE software for the MnAs compounds are presented. For isotropic systems, the structure should display a spherical (3D) or circular (2D) shape in nature. However, any deviation from this shape means anisotropy. Hence, Fig. 3 and Fig. 4 confirm the anisotropic nature displayed by the calculated mechanical parameters in Table 3. Meanwhile, when comparing the 3D and 2D surface plots in Fig. 3 with Table 3, the cP phase exhibits a lower overall stiffness due to its larger multi-membered edge outshoot that introduces high structural flexibility. Similarly, comparing the Tetr phase (having a modulus stiffness of 175.2 GPa) with the hcp phase (of modulus 189.6 GPa), the hcp presents a comparable but slightly wider range of mechanical responses, indicating that its impervious nature enhances low flexibility while maintaining sufficient rigidity for structural stability. The Poisson's ratio distribution shown in Fig. 4 quantifies the material's lateral response to applied strain. The plot exhibits a fourfold symmetry, exhibiting the expected directional-dependent deformation behavior and highlighting its significant mechanical anisotropy. The variation in Poisson's ratio across different orientations suggests that all three phases underwent non-uniform lateral deformation regardless of the crystal topology and anisotropic bonding environment.

Table 3: Calculated average values based on the VRH approximation for Bulk modulus (B_H), Shear modulus (G_H), and Young's modulus (E_H) in GPa, Poisson's ratio (V_H), Pugh's ratio (B_H/G_H), Universal anisotropy index (A^U), anisotropy indices of shear (A^G) and bulk (A^B), scalar log-Euclidean anisotropy index (A^L) and Zener anisotropy factor (A^z) moduli

MnAs Phases	Tetr	hcp	cP
B_V	193.02	171.78	56.76
B_R	185.02	175.44	56.76
B_H	189.02	173.61	56.76
G_V	66.10	58.90	9.61
G_R	64.11	85.50	25.37
G_H	65.10	72.20	9.25
E_V	177.98	158.56	27.30
E_R	172.42	220.65	88.97
E_H	175.20	189.60	26.33
V_V	0.35	0.35	0.42
V_R	0.34	0.29	0.42
V_H	0.35	0.31	0.42
B_H/G_H	2.90	2.40	6.13
A^U	0.20	-1.58	-3.11
A^G	0.02	-0.18	-0.45
A^B	0.02	-0.01	0.01
A^L	0.05	0.72	2.17
A^z	0.77	4.50	0.57

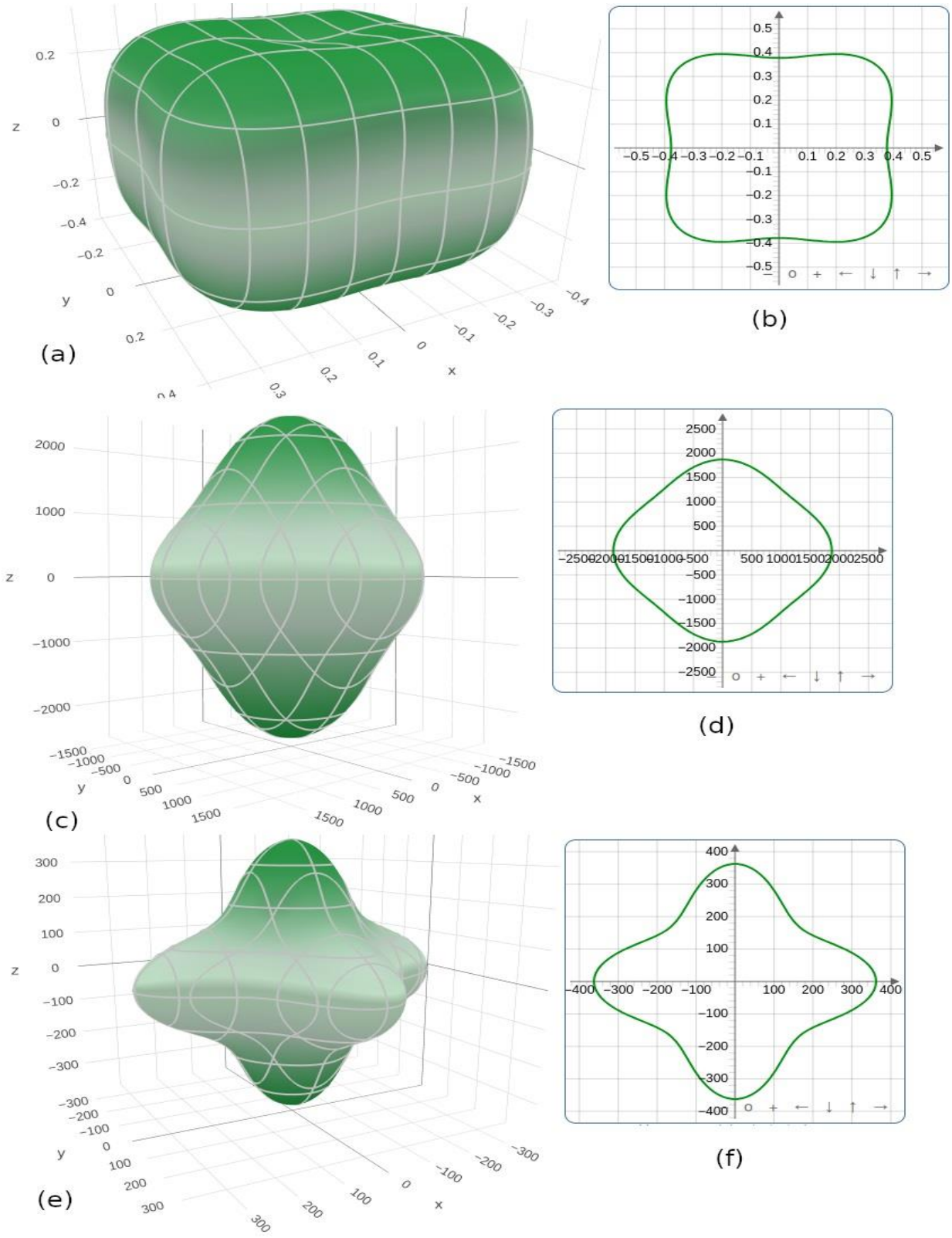

Fig. 3: Young modulus representations in 3D directional (Fig. 3(a, c, e)) and xy-surface (Fig. 3(b, d, f)) dependence of Tetr, hcp, and cP phases of MnAs

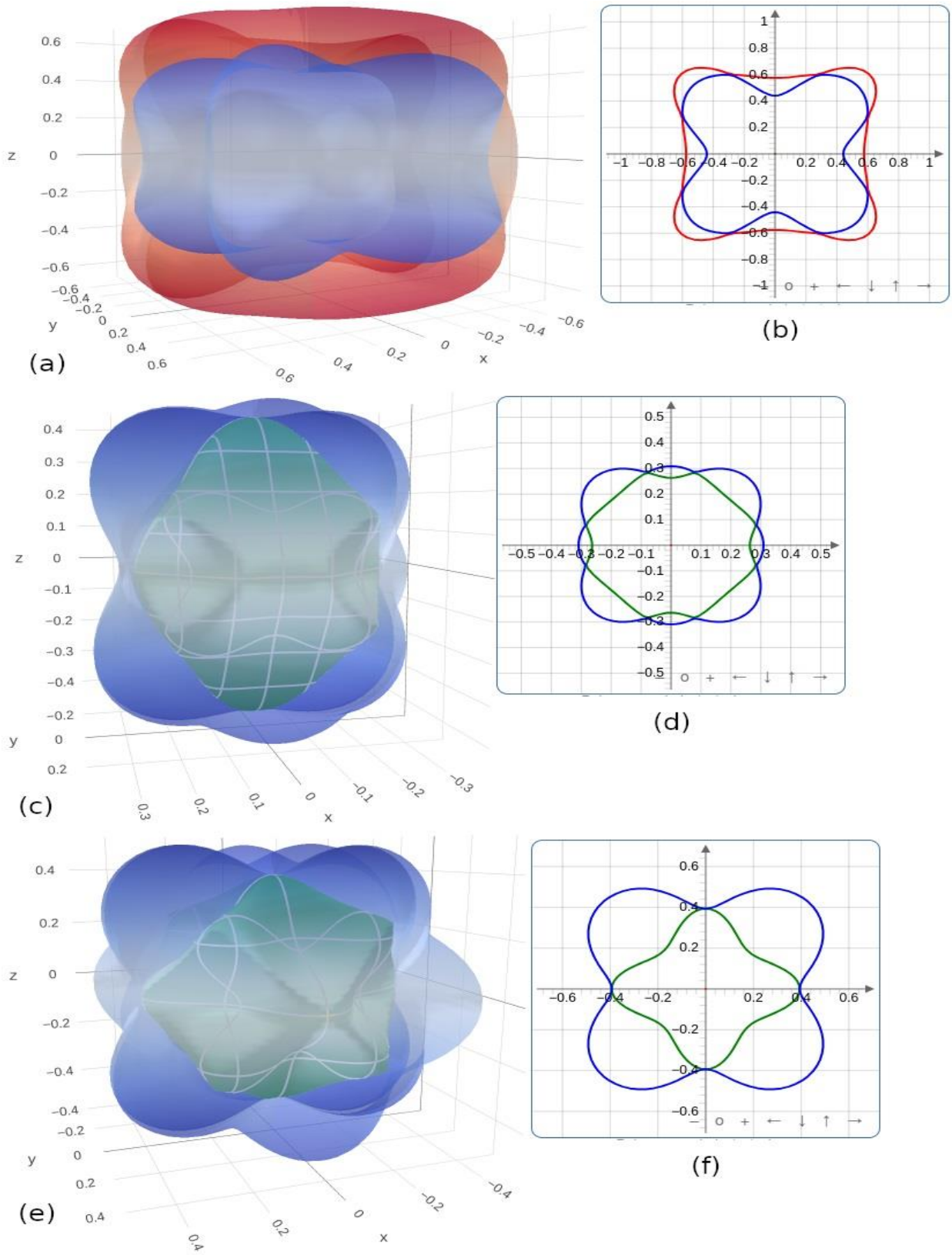

Fig. 4: Poisson ratio representations in 3D directional (Fig. 4(a, c, e)) and xy-surface (Fig. 4(b, d, f)) dependence of Tetr, hcp, and cP phases of MnAs

3.4 Thermoelectric Transport Properties

In Fig. 5, the thermoelectric transport properties for the three phases of MnAs are well presented. Comparing these properties to other known thermoelectric materials can help contextualize their potential. The dependence of the Seebeck coefficient (top panels), electrical conductivity (middle panels), and power factor (bottom

panels) on chemical potential at varying temperatures is discussed.

The Seebeck effect generates voltages from temperature differences. The response of the Seebeck coefficient *S* to the applied temperature gradient is given by $S = V/\Delta T$, where V is the voltage, and ΔT is the temperature difference. When two different conductors are kept at different temperatures, the electrons on the hot end have higher thermal energy than the electrons on the cold end. Consequently, electrons will flow towards the colder end. This net accumulation of electrons at the colder end creates a potential difference across the conductor, with the cold end negative. Moreso, high Seebeck coefficient *(S)* materials yield high power factor (PF) and figure of merit (Z_T), signifying greater capability to convert waste heat into useful electrical energy (Aliabad *et al*., 2012). A negative *S* value denotes n-carriers, while a positive *S* value denotes p-carriers. Chemical potential $(\varepsilon - \varepsilon_0)$ determines the concentration of charge carriers in materials. In Fig. 5(a, d, g), the *S* profiles of the Tetr, hcp, and cP phases as a function of chemical potential are shown for different temperatures. Also, the wavelike display of *S* shows high and low peaks at different temperatures. The figures display the highest *S* value for the three phases in the p-type region as 32.6 μV/K at 800 K (Tetr), 48.3 μV/K at 800 K (hcp), and 1500.0 μV/K at 300 K (cP), respectively. Similarly, in the region of n-type, the maximum *S* value for the same order are -44.6 μV/K, -43.8 μV/K, and -1570.3 μV/K respectively. From the figures, it is clear that the Tetr and hcp phases are high-temperature materials, and that the former is an n-type carrier while the latter is a p-type carrier. Further, the room-temperature (300 K) cP phase is an n-type alloy. One deduction from these results is that, apart from the high mechanical strength and deformability, the cubic cP phase exhibits, at 300 K, the highest and lowest Seebeck coefficients, suggesting that this phase is a good candidate for thermoelectricity. This behavior of the cP phase confirms the predictions of a sharp, high-slope feature in the Total-DOS around the Fermi level in Fig. 2(c).

Electrical conductivity is the movement of electrical charge in a substance. Materials with high electrical conductivity are necessary to minimize heating of the conductor from current flow (Joule heating). Charge carriers in metallic compounds are electrons, whereas in semiconductors, holes and electrons are in charge (Qasimullah *et al.*, 2024). Fig. 5(b, e, h) illustrates the relationship between electrical conductivity per relaxation time (σ/τ) and chemical potential at different temperatures for the intermetallic MnAs alloys. The three phases of MnAs displayed alignment in their electrical conductivity for all temperatures. The figures show that σ/τ decreases with increasing temperature. The maximum calculated value of σ/τ for Tetr, hcp, and cP phases are 37.7 x 10^{19} 1/Ω.cm.s, 56.2 x 10^{19} 1/Ω.cm.s, and 58.3 x 10^{19} 1/Ω.cm.s, respectively. Meanwhile, σ/τ shows both negative and positive gradients across the energy range in the Tetr and hcp phases. In contrast, a positive gradient is sustained in the cP phase in almost all energy scenarios.

In Fig. 5(c, f, i), the variation of the power factor (PF) with chemical potential energy at different temperatures is shown. The power factor is related to the Seebeck coefficient and electrical conductivity by $PF = S^2\sigma/\tau$ in units of $W.cm^{-1}.K^{-2}.s^{-1}$. The characteristic behavior of PF for the three alloys is shown in the bottom panel of Fig. 5. The maximum PF is recorded at 800 K, which is 4.4 x 10^{11} $W.cm^{-1}.K^{-2}.s^{-1}$ and 7.2 x 10^{11} $W.cm^{-1}.K^{-2}.s^{-1}$ for the Tetr and hcp phases, while the cP phase is 9.4 x 10^{11} $W.cm^{-1}.K^{-2}.s^{-1}$, respectively. The nature of the PF for cP > hcp > Tetr is attributed to variation in the chemical potential energy. The values for the Tetr phase lie between 0.1 – 0.12 Ry, the hcp phase lies between 0.11 – 0.13 Ry, while that of the cP phase is between 0 – 0.02 Ry. Furthermore, the minimum PF occurred at 300

K as 0.1 x 10^{11} W.cm^{-1}.K^{-2}.s^{-1} (for Tetr phase), 0.23 x 10^{11} W.cm^{-1}.K^{-2}.s^{-1} (for hcp phase), and 1.0 x 10^{11} W.cm^{-1}.K^{-2}.s^{-1} (for cP phase). The trend observed in the cubic MnAs phase has also been observed in other cubic materials (Adeyemo *et al*., 2025; Ramanathan *et al*., 2017).

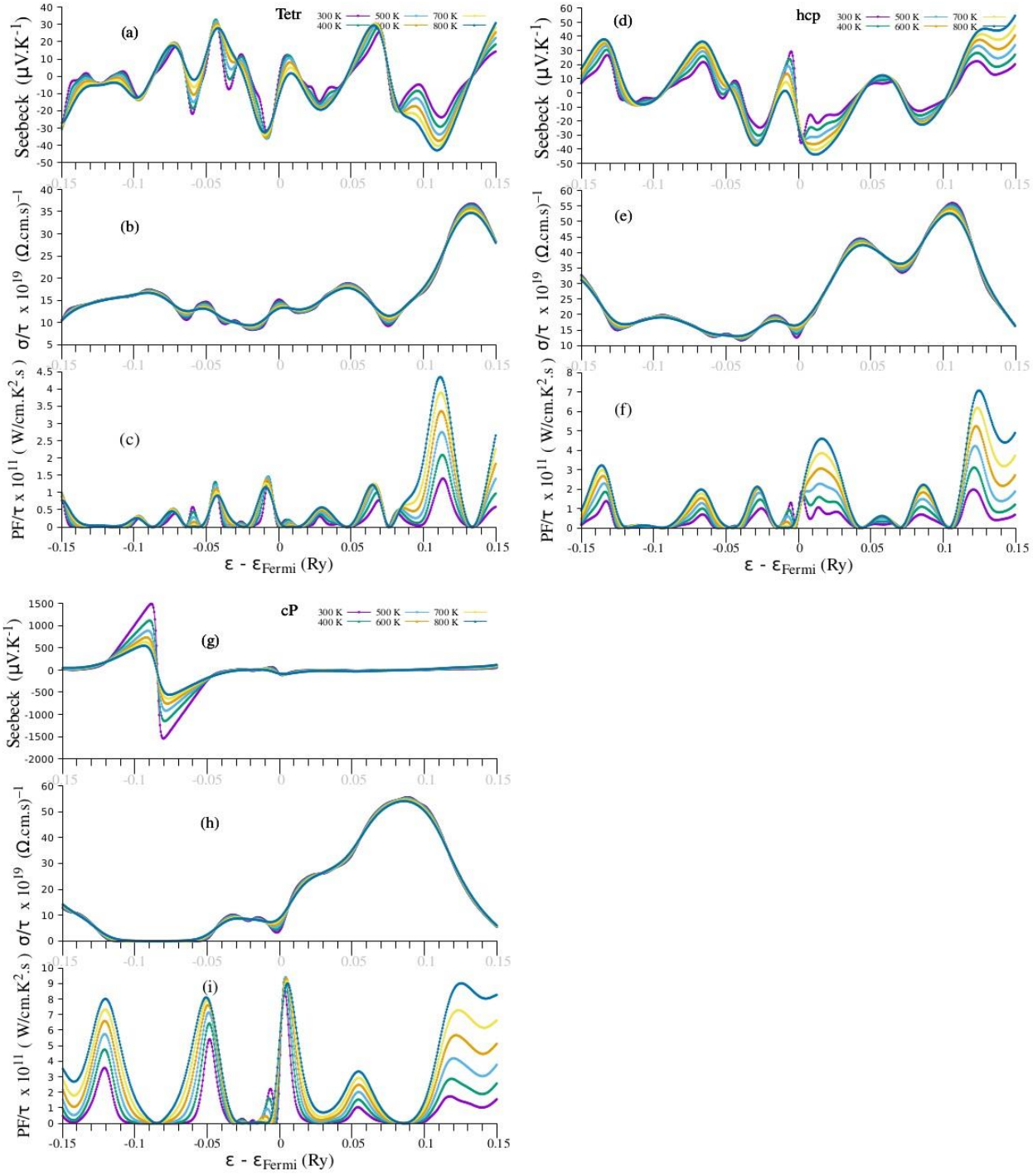

Fig. 5: Seebeck coefficient, Electrical conductivity and Power factor as a function of chemical potential $(\varepsilon - \varepsilon_0)$ for the Tetr, hcp, and cP phases of MnAs

Fig. 6 present plots of thermal conductivity k_e versus $(\varepsilon - \varepsilon_0)$) temperature. From the illustration, Fig. 6(a) depicts the Tetr-phase, Fig. 6(b) depicts the hcp-phase, and Fig. 6(c) depicts the cP-phase. It is well known that a better TE device will exhibit a minimum k_e value, thereby

improving efficiency. In this assessment, we compute using Eq. (5) the k_e dependence at different temperatures for specific $(\varepsilon - \varepsilon_0)$ values ranging from –0.15 Ry to +0.15 Ry, respectively. The lowest value of k_e across all three phases is observed at 300 K, with the least being the cubic cP phase in Fig. 6(c). This behavior at 300 K justifies the high Seebeck coefficient observed in Fig. 5(g) at the same temperature, thus demonstrating the cubic cP phase as promising for TE applications.

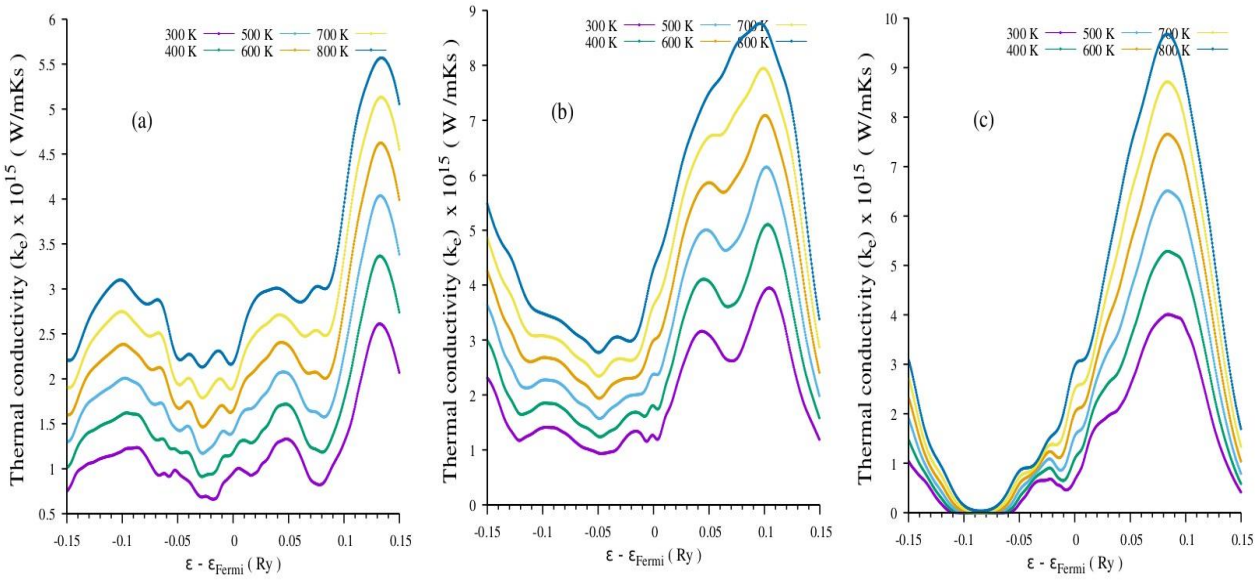

Fig. 6: Thermal conductivity versus chemical potential $(\varepsilon - \varepsilon_0)$ for Tetr, hcp, and cP phases of MnAs

3.5 Thermophysical Properties

Thermophysical calculations have been performed using the quasi-harmonic Debye model, which has been successfully applied to estimate the thermodynamic properties of various materials (Meziany *et al*., 2025; Akpan *et al*., 2025; Ekwere *et al*., 2024). Thermodynamic properties elucidate essential industrial applications and can extend our knowledge of materials' behavior under different environmental conditions. The procedure requires only energy-volume data to calculate the Debye temperature, θ_D, which can be interpreted as the temperature at which the highest-frequency mode is excited. This is of great significance to predicting the heat capacity, as well as the internal and free energies at any temperature in an atomic solid. The standard Debye temperature formula to evaluate is given by (Zheng *et al*., 2015):

$$\Theta_D = \frac{h}{k_B}\left[\frac{3n}{4\pi}\left(\frac{N_A\rho}{M}\right)\right]^{\frac{1}{3}} . v_m \qquad (20)$$

where h is the Planck's constant, k_B is the Boltzmann's constant, n is the number of atoms per formula unit, N_A, M, and ρ denotes Avogadro's number, molar mass, and density. The average acoustic sound velocity v_m is described as:

$$v_m = \left[\frac{1}{3}\left(\frac{2}{v_t^3} + \frac{1}{v_l^3}\right)\right]^{-1/3} \qquad (21)$$

$$\text{with } v_t = \sqrt{\frac{G_H}{\rho}} \text{ and } v_l = \sqrt{\frac{3B_H + 4G_H}{3\rho}} \qquad (22)$$

where v_t and v_l are achieved from Navier's equation as the transverse and longitudinal elastic wave velocities. The calculated quasi-harmonic Debye temperature at T = 0 K and P = 0 GPa is 393.101 K (Tetr phase), 91.807 K (hcp phase), and 161.072 K (cP phase), which in similar order are in good agreement with the mechanically obtained Debye temperature θ_D = 406.571 K, θ_D = 94.887 K, and θ_D = 164.488 K evaluated from Eq. (20) [see Table 4]. Such low θ_D values can be attributed to the high molecular weight and low density of the MnAs alloys,

suggesting that the compounds are likely brittle crystals at room temperature. The calculated densities (ρ) of the compounds range from 7.242 to 4.682 g/cm^3 in the order of Tetr > hcp > cP, respectively. From Table 4, the melting temperatures (T_m) of the different phases follow the same ordered trend as the density, indicating that the cP phase will undergo a faster transformation from the solid to the gas state than the Tetr and hcp phases. Further, the nature of the θ_D is also hallmarked by the crystal's hardness as showcased in Table 3 above. Meanwhile, the computed densities (ρ) reported herein decreased from the Tetr-phase to the cP-phase. This effect can be attributed to the increasing power factor (PF) shown in Fig. 5.

Table 4: The calculated acoustic compressional (V_C), bulk (V_B), shear (V_S), and average (V_m) sound velocities (in m/s), Debye temperature θ_D (K), melting temperature T_m (K), density ρ (in g.cm^{-3}) and the Dulong-Petit limit (Cal./mol.K) of the Tetr, hcp and cP phases of MnAs intermetallic compounds

MnAs phases	V_L	V_B	V_T	V_m	θ_D	T_m	ρ	Dulong-Petit limit	Ref.
Tetr	5868.589	4858.133	2851.138	3192.058	406.571	1594.145	7.2422	35.06	This work
hcp	5979.840	4796.206	3092.923	773.323	94.887	1070.640	6.839	24.37	This work
cP	3723.460	3374.652	1362.683	1539.359	164.488	990.990	4.682	47.46	This work

Nevertheless, as a crucial thermophysical property of solids, θ_D is connected to many physical factors, including vacancy formation energy, entropy, melting temperature, atomic bonding strength, vibrational specific heat, internal and free energies, etc. (Meziany *et al*., 2025). Depicted in Fig. 7 are the computed internal energy, free energy, entropy, and constant volume heat capacity, C_V, in the temperature ranges of 0 to 800 K. The variation profiles in Fig. 7 exhibit subtle differences in behavior as temperature increases. The internal and free energies are two fundamental thermodynamic quantities that govern oscillations around equilibrium positions in systems. While the former depicts the amount of heat energy internal to the system and available for thermodynamic interaction with the surroundings, the latter (free energy) quantifies the heat energy the system can absorb from external sources. Fig. 7(a) showcases the temperature dependence of both the internal energy (dotted-dash lines) and free energy (solid lines) of the three phases of MnAs. The internal energy at temperatures above 60 K increases linearly with rising temperature. The free energy, on the other hand, appears increasingly negative with rising temperature. The more negative the free energy of the materials, the more likely they are to demonstrate superior thermal performance. This indication improves the thermodynamic stability at elevated temperatures. Fig. 7(b) illustrates how the entropies of the alloys rise with temperature. Moreover, since free energy is derived from entropy, higher entropies correspond to an increasing negative free energy. The plots of entropy changes with temperature show a continuous increase in the entropies of the compounds. In Fig. 7(c), the heat capacity C_V is the heat retention ability of a compound showcased in the order of hcp < Tetr < cP, within the expected range from 0 K to 800 K.

From our observation, the incremental changes in internal energy of the compounds equivalently yield higher C_V values. This indication may result from the low-frequency modes at low temperature, where only acoustic modes contribute to vibrational excitations. However, Fig. 7(c) shows a notable rise in C_V between 6 and 50 K. Meanwhile, a gradual increase up to 200 K is observed for the Tetr

phase of MnAs, whereas the hcp and cP phases display sharp increases up to 42 K and 98 K, respectively. At Dulong–Petit limit, the recorded C_V values are 35.06 Cal./mol.K (Tetr phase), 24.37 Cal./mol.K (hcp phase), and 47.46 Cal./mol.K (cP phase). Consequently, although the C_V profile for all phases is preserved even below room temperature (300 K) in the Dulong-Petti limit, the cP phase among the three phases exhibits much greater thermal robustness.

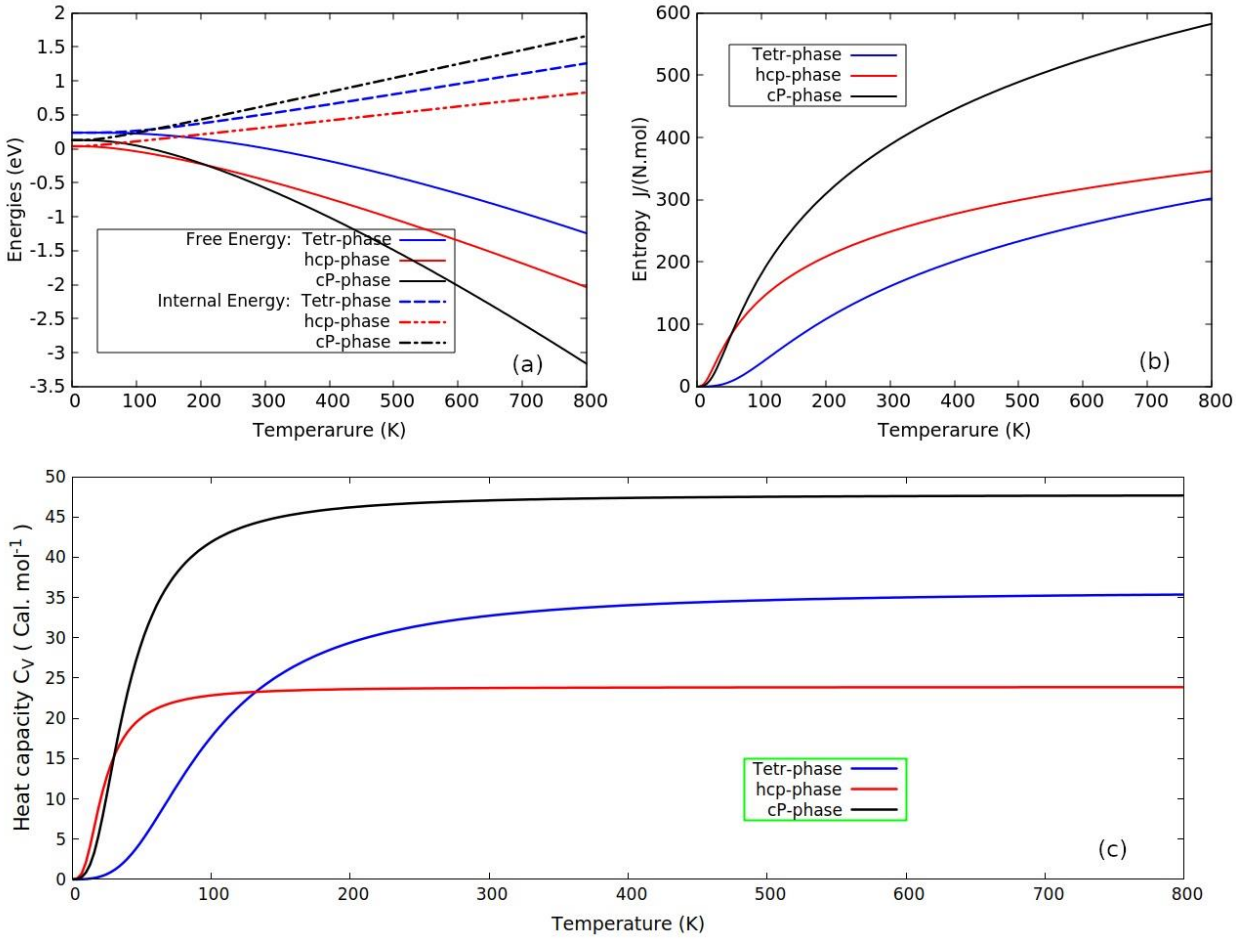

Fig. 7: Temperature dependence of free energy (a), heat capacity (b), and entropy for Tetr-, hcp- and cP-phases of MnAs compounds

4.0 Concluding Remarks

This investigation compares the tetragonal (Tetr), hexagonal (hcp), and cubic (cP) phases of MnAs intermetallics by examining their electronic, thermoelectric, mechanical, and thermophysical properties. The results highlight the coexistence of Tetr, hcp, and cP phases, with the hcp phase being more thermodynamically stable at lower temperatures. The thermoelectric analysis of the MnAs phases is investigated herein for the first time, and is open for criticism. Using Vanderbilt-type ultrasoft pseudopotentials (USPPs) within the PBEsol exchange-correlation as implemented in the quantum ESPRESSO code, we studied the compounds. The structural properties of the three alloys accounted for the formation energy and binding energy respectively. The calculated lattice parameters are in good agreement with experiment. The bound state, minimum energy, reveals cP (-916.52 Ry) < Tetr (-880.61 Ry) < hcp (-458.51 Ry). The electronic properties shows that the compounds are metals and exhibit promising electronic transport near the Fermi level. The calculated elastic constants satisfy the Born stability criteria and predict the mechanically that the compounds are anisotropic alloys. Furthermore, the Poisson's

and Pugh's ratios results reaffirm the DOS analysis that the compounds are ductile with metallic bonding between atoms. The highest power factor displayed was found in the cubic cP phase. Since no experimental work on thermoelectric transport has been reported, we strongly recommend and urge further experimental investigations to validate our findings. Knowing that there were no usable experimental results for the elastic and thermoelectric behaviors concerning tetragonal and cubic phases of MnAs alloys, our reported values appreciably become the only available results in this regard. The thermophysical assessment of the alloys show that the melting temperature increases with density. In summary, the interplay among the electronic, thermoelectric, mechanical, and thermophysical properties of the three phases of MnAs makes them attractive for various applications in energy-harvesting systems, with the cP phase offering significant advantages in Seebeck effects and conductive flexibility.

Reference

Adeyemo, P. A., Ogunremi, K. J., Bankole, T. P., Egunjobi, A. I., Solola, G. T. & Adebambo, P. O. (2025). Structural, electronic and thermoelectric properties of NiScBi and PdScBi Half-Heusler alloys from first principles. *J. Phys. Chem. Solids*, 199, 112488.

Akpan, A. O., Ekong, S. A., & Emah, J.B., (2025). Low pressure-induced phase transition study of α-AlH_3 and its hydrogen storage evaluation for energy applications via electronic, structural, thermodynamic and optical analysis. *Res. J. Sci. Techn.*, 5 (7), 1.

Algarni, H., Gueddim, A., Bouarissa, N., & Khan, M. A. (2020). Electronic properties, optical spectra and magneti sation of MnAs material under compression. *Philosophical Magazine, 100*(23), 2972.

Aliabad, H. R., Ghazanfari, M., Ahmad, I., & Saeed, M. (2012). Ab initio calculations of structural, optical and thermoelectric properties for $CoSb_3$ and ACo_4Sb_{12} (A= La, Tl and Y) compounds. *Comput. Mater. Sci*, 65, 509.

Arejdal, M., Bahmad, L., & Benyoussef, A. (2017). The calculated magnetic properties and magneto-caloric effect in compound MnAs. *J. Supercond. Nov. Magn.* 30, 1565.

Balaji, A.S., Ramasamy, A., Sivasankar, K.J., Mohanraj, H.R., & Thiruvadigal-D, J. (2025). DFT+NEGF insights on boosting the thermoelectric figure of merit of 2D GeTe/arsenene vdW heterostructure device: Interface engineering, *Surfaces and Interfaces*, 56, 105534.

Baroni, S., Giannozzi, P., & Isaev, E. (2010). Density-functional perturbation theory for quasi-harmonic calculations, *Rev. Mineral. Geochem.* 71 (1), 39.

Born, M., Huang, K., & Lax, M. (1955). Dynamical theory of crystal lattices. *Am. J. Phys.*, 23 (7), 474.

Chen, X., Zhang, X., Gao, J., Li, Q., Shao, Z., Lin, H., & Pan, M. (2021). Computational Search for Better Thermoelectric Performance in Nickel-Based Half-Heusler Compounds. *ACS Omega*, 6, 18269.

Chenafi, M.A., Boucif, A., Mellah, D.E., & Demmouche, K. (2025). First-principles calculation of structural and optoelectronic properties of Cu_2MgSnS_4 (CMTS): critical insights from meta-GGA. *Phys. Scr.* 100, 075943.

Ekong, S.A., Adebambo, P.O., Adetunji, B.I., Uto, O.T., & Adebayo, G.A. (2025). Electronic, mechanical, dynamical, thermodynamic and thermoelectric study of ScNiSb Heusler-like alloy: planewave

density functional theory approach, *Discover Chemistry*, 2, 344.

Ekong, S.A., Fuwape, I.A. & Odo, E.A. (2014). Ab initio study of the electronic structure of silicon quantum dots. *J. Nig. Asso. Math. Phys.*, 26, 177.

Ekong, S.A., Oloye, M.T. & Oyegoke, D.A. (2015). Ground-state energy calculation of helium atom using quantum Monte Carlo casino-code, *Adv. Phys. Theo. Appl*. 46 (1), 1.

Ekwere, E.J., Emah, J.B. & Ekong, S.A. (2024). Structural, Electronic, Thermophysical and Optical Investigation of Tetragonal ($C11_b$ – $CrSi_2$) Material: A Theoretical Analysis, *Res. J. Sci. Techn.*, 4(4), 23.

Espinosa-García, W., Ruiz-Tobón, C., & Osorio-Guillén, J. (2011). The elastic and bonding properties of the sulvanite compounds: A first-principles study by local and semi-local functionals, *Physica B Condens. Matter* 406 (20), 3788.

Gaillac, R., Pullumbi, P., & Coudert, F.-X. (2016). ELATE: An Open-Source Online Application for Analysis and Visualization of Elastic Tensors. *J. Phys.: Condens.Matter*, 28, 275201.

Gama, S., & Cardoso, L.P. (2006). Structural and Magnetic Study of the MnAs Magnetocaloric Compound. *Materials Research*, Vol. 9, No. 1, 111.

Giannozzi, P., Andreussi, O., Brumme, T., Bunau, O., Nardelli, M.B., Calandra, M., Car, R., Cavazzoni,C., Ceresoli, D., Cococcioni, M., Colonna, N., Carnimeo, I., Corso, A. D., Gironcoli, S. de, Delugas, P., DiStasio Jr, R.A., Ferretti, A., Floris, A., Fratesi, G., Fugallo, G., Gebauer, R., Gerstmann, U., Giustino, F., Gorni, T., Jia, J., Kawamura, M., Ko, H-Y., Kokalj, A., Küçükbenli, E., Lazzeri, M., Marsili, M., Marzari, N., Mauri, F., Nguyen, N.L., Nguyen, H-V., Roza, A. O. D-l, Paulatto, L., Poncé, S., Rocca, D., Sabatini, R., Santra, B., Schlipf, M., Seitsonen, A.P., Smogunov, A., Timrov, I., Thonhauser, T., Umari, P., Vast, N., Wu, X., & Baroni, S., (2017). Advanced capabilities for materials modelling with QUANTUM ESPRESSO, *J. Phys.*: Condens. Matter 29 (46), 465901.

Gourdon, O, Gout, D., & Miller, G.J. (2016). Reference Module in Materials Science and Materials Engineering, Intermetallic Compounds, Electronic States of. https://doi.org/10.1016/B978-0-12-803581-8.01049-3

Greaves, G.N., Greer, A.L., Lakes, R.S., Rouxel, T. (2011). Poisson's ratio and modern materials. *Nat. Mater.*, 10, 823.

Gregory, E.E., Ekong, S.A., & Emah, J.B. (2024). Ab-initio assessment of the electronic, mechanical, thermal, optical and phonon properties of B3-AlAs, *Res. J. Sci. Techn.*, 4 (3), 69.

Habiba, U., Khattak, K.S., Ali, S., & Khan, Z.H. (2020). MnAs and $MnFeP_{1-x}As_x$-based magnetic refrigerants: a review. *Mater. Res. Express,* 7, 046106.

Hagedorn, M.F., & Jeitschko, W. (1995). Synthesis and Crystal Structure of Mn4As3 and Its Relation to Other Manganese Arsenides. *J. Solis State Chemistry*, 119, 344.

Hayashi, T., Hashimoto, Y., Katsumuoto, S., & Iye, Y. (2001). Effect of low-temperature annealing on transport and magnetism of diluted magnetic semiconductor (Ga,Mn)As, *Appl. Phys. Letts*. 78, 1691.

Hayat, M.S., Khalil, R.M.A., Hassan, R.U., Rehman, A.u., Alanazi, Y.M., & Yuennan, J. (2025). The Ab-initio investigation of structural, electronic, mechanical, dynamical and

thermodynamic properties of double halide $Cs_2SrTaCl_6$, $Cs_2SrTaBr_6$, and $Cs_2BaTaBr_6$ perovskites: A Dispersion Corrected DFT Study, *J. Inorgan. Organometal. Polyme. Mater.*, https://doi.org/10.1007/s10904-025-03780-x

Hill, R. (1952). The Elastic Behaviour of a Crystalline Aggregate. *Proc. Phys. Soc.*, Section A 65, 349.

Jolayemi, O.R. & Ekong, S.A. (2020). Electronic, structural, magnetic and mechanical properties of $Mg_{1-x}Sr_xN$ rocksalt from first-principles, *Tran. Nig. Asso. Math. Phys*. 13, 39.

Jolayemi, O.R., Ekong, S.A., Adetunji, B.I. & Iboh U.A. (2019). First-principles study of half-metallic ferromagnetism in (1 1 1) Surface of csse. *J. Nig. Asso. Math. Phys.*, 51, 157.

Khan, B., Aliabad, H.A.R., Khan, I., Jalali-Asadabadi, S., & Ahmad, I. (2017). Comparative study of thermoelectric properties of Co based filled antimonide skutterudites with and without SOC effect, *Compt. Mater. Sci.* 131, 308.

Li, W., Dong, H., Zhang, B., Zou, S., Mu, W., & Cai, Y. (2024). The Influence of Adjustable Ring-Mode Laser on the Formation of Intermetallic Compounds and Mechanical Properties of Ultra-Thin Al-Cu Lap Welded Joints. *J. Mater. Process. Technol.*, 332, 118537.

Luan, X., Qin, H., Liu, F., Dai, Z., Yi, Y., & Li, Q. (2018). The Mechanical Properties and Elastic Anisotropies of Cubic Ni3Al from First Principles Calculations, *Crystals*, 8, 307.

Madsen, G.K., & Singh, D.J. (2006). BoltzTraP. A code for calculating band-structure dependent quantities. *Comput. Phys. Commun.* 175, 67.

Maki, K., Kaneko, T., Hiroyoshi, H., & Kamigaki, K. (1998). Crystalline and magnetic properties of MnAs under pressure. *J. Magn. Magn. Mater*. 177–181, 1361.

Malica, C. & Corso, A.D. (2020). Quasi-harmonic temperature dependent elastic constants: applications to silicon, aluminum, and silver. *J. Phys.: Condens. Matt.*, 32 (31), 315902.

Marenkin, S.F., Kochura, A.V., Izotov, A.D., & Vasilev, M.G. (2018). Manganese Pnictides MnP, MnAs, and MnSb are Ferromagnetic Semimetals: Preparation, Structure, and Properties (a Survey). *Russ. J. Inorg. Chem.* **63** (14), 1753.

Meziany, A., Essami, M., Alaoui, S.M.A.E., Didi, Y., Lazrak, M., Touti, R., Tahiri, A., & Naji, M. (2025). Toward Lightweight Solid-State Hydrogen Storage: Computational Investigation of Potassium Antiperovskites. *Phys. Status Solidi* A, 2500168.

Moradiannejad, F., Hashemifar, S.J., & Akbarzadeh, H. (2013). The effect of pressure on electronic and magnetic properties of MnAs crystal. *J. Compt. Methods Phys.*, 24, 879164.

Mouhat, F., & Couder, F. (2014). Necessary and sufficient elastic stability conditions in various crystal systems, *Phys. Rev.* B 90, 224104.

Murnaghan, F.D. (1944). The compressibility of media under extreme pressures, *Proc. Natl Acad. Sci.,* 30, 244.

Ohno, H. (1999). Properties of ferromagnetic III-V semiconductors, *J. Magnet. Magn. Mater*., 200, 110.

Omboga, N.K., Otieno, C.O. & Nyawere, P.W.O. (2020). First principle study of the mechanical and phonon dispersion of the iron pnictide compound $EuFe_2As_2$. *The Scientific World J.*, Vol. 2020, 5986073.

Osorio-Guillén, J. M., & Espinosa-García, W. F. (2012). A first-principles study of the electronic structure of the sulvanite compounds, *Physica B Condens. Matter* 407, 985.

Paiva, R.D., Alves, J.L.A., Nogueira, R.A., Leite, J.R., & Scolfaro, L.M.R. (2004). First-principles materials study for spintronics: MnAs and MnN. Braz. *J. Phys*. 34, 568.

Pugh, S.F. (1954). XCII. Relations between the elastic moduli and the plastic properties of polycrystalline pure metals, *Philosophical Magazine Series* 7 (45), 367, 823.

Qasimullah, M.I., Rahman, W.U., Shehzad, N., Ilyas, M., & Ahmad, M. (2024). Theoretical studies of the electronic and thermoelectric properties of $PrIn_3$ and $NdIn_3$ in cubic phase, *J. Mater. Sci. Nanotech.,* 12 (2), 202.

Qian, M.C., Fong, C.Y., Pickett, W.E., & Wang, H.Y. (2004). An ab initio investigation on the zinc-blende MnAs nanocrystallite. *J. Appl. Phys.*, 95(11), 7459.

Ramanathan, A.A. & Khalifeh, J.M. (2017). Enhanced thermoelectric properties of suspended mono and bilayer of MoS_2 from first principles. *TNANO*, 00728.

Ranganathan, S.I. & Ostoja-Starzewski, M. (2008). Universal Elastic Anisotropy Index. *Phys. Rev. Lett.,* 101, 055504.

Reuss, A. (1929). Berechnung der Fließgrenze von Mischkristallen auf Grund der Plastizitätsbedingung für Einkristalle. ZAMM - J. Appld. Math. & Mechan. / Zeitschrift für Angewandte Mathematik und Mechanik 9, 49.

Sanvito, S., & Hill, N.A. (2000). Ground state of half-metallic zinc-blende MnAs. *Phys. Rev.* B, 62(23), 15553.

Saypulaeva, L.A., Gadzhialiev, M.M., Alibekov, A.G., Melnikova, N.V., Zakhvalinskii, V.S., Ril, A.I, Marenkin, S.F., Efendieva, T.N., Fedorchenko, I.V., & Mollaev, A. Y. (2019). Effect of Hydrostatic Pressures of up to 9 GPa on the Galvanomagnetic Properties of Cd_3As_2–MnAs (20 mol % MnAs) Alloy in a Transverse Magnetic Field. *Inorg Mater* **55**, 873.

Tocado, L., Palacios, E., & Burriel, R. (2009). Entropy determinations and magnetocaloric parameters in systems with first-order transitions: Study of MnAs. *J. Appl. Phys*. 105, 093918.

Tolochyn, O.I., Baglyuk, G.A., & Tolochyna, O.V. (2021). Structure and Physicomechanical Properties of the Fe_3Al Intermetallic Compound Obtained by Impact Hot Compaction. *Mater. Sci.*, 56, 499.

Voigt, W., (1928). J. Leherbuch de Kistallphysik.: 739; Voigt, W. (1910). Lehrbuch der kristallphysik (mit ausschluss der kristalloptik). B.G. Teubner, Leipzig, Berlin.

Yu, C.-F., & Liu, Y.-L. (2025). DFT study of Au_3In and Au_3In_2 intermetallic compounds: Structural Stability, Fracture Toughness, Anisotropic Elasticity, and Thermophysical Properties for Advanced Applications. *Materials*, 18, 1561.

Yu, C.F., Peng, J.W., Hsiao, C.C., Wang, C.H., & Lo, W.C. (2025). Development of GUI-Driven AI Deep Learning Platform for Predicting Warpage Behavior of Fan-Out Wafer-Level Packaging. *Micromachines,* 16, 342.

Zeng, X., Rufang, P., Yanlin, Y., Zuofu, H., Yufeng, W., & Lin, S. (2018). Pressure Effect on Elastic Constants and Related Properties of Ti3Al Intermetallic

Compound: A First-Principles Study, *Materials*, 11.

Zheng, B., Zhang, M. & Luo, H-G. (2015). Pressure effect on structural, elastic and thermodynamic properties of tetragonal B_4C_4. AIP Advances **5**, 037123.